







# Excitation of high order orbital angular momentum modes in ultra-short chiral long period fiber gratings

ZHENG HUANG,<sup>1,2</sup> ZHIYONG BAI,<sup>1,2,\*</sup>  GUOXUAN ZHU,<sup>1,2</sup> CHUROU HUANG,<sup>1,2</sup> JIAYAN CHEN,<sup>1</sup> SHEN LIU,<sup>1,2</sup>  CAILING FU,<sup>1,2</sup>  JUN HE,<sup>1,2</sup>  AND YIPING WANG<sup>1,2</sup>

<sup>1</sup>Key Laboratory of Optoelectronic Devices and Systems of Ministry of Education/Guangdong Province, College of Physics and Optoelectronic Engineering, Shenzhen University, Shenzhen 518060, China

<sup>2</sup>Shenzhen Key Laboratory of Photonic Devices and Sensing Systems for Internet of Things, Guangdong and Hong Kong Joint Research Centre for Optical Fibre Sensors, Shenzhen University, Shenzhen 518060, China

\*baizhiyong@szu.edu.cn

**Abstract:** A class of ultra-short chiral long period fiber gratings (CLPFGs) are prepared by writing a spiral curve on the surface of a six-mode fiber. The CLPFGs are applied to excite  $\pm 2^{\text{nd}}$ - and  $\pm 3^{\text{rd}}$ -order orbital angular momentum (OAM) modes. The coupling efficiency of the CLPFG in these modes can be as high as 99%, when the length is only 0.5cm. The polarization characteristic of the excited higher-order OAM modes in CLPFGs was theoretically analyzed and experimentally investigated. Results show that the obtained  $\pm 2^{\text{nd}}$ - and  $\pm 3^{\text{rd}}$ -order OAM modes are polarization independent, as expected.

© 2021 Optical Society of America under the terms of the [OSA Open Access Publishing Agreement](#)

## 1. Introduction

Orbital angular momentum (OAM) is an extrinsic property of light. The light beam carrying OAM shows an azimuthal phase dependence  $\exp(il\varphi)$ , where  $\varphi$  is the azimuthal angle and  $l$  is the topological charge number. This kind of phase structure creates an OAM beam with a helical wavefront, a phase singularity in the center, and a donut-shaped intensity distribution. As a result, the OAM beam has been extensively investigated to excavate its potential applications in multiple fields.

For instance, the helical wavefront was used in a tweezers system to rotate the particles [1]. The donut-shaped intensity profile and phase singularity was used to enhance imaging of a weak light field [2,3]. Due to the infinity modes and excellent orthogonality between them, OAM modes has been used in optical communication systems with a large capacity and a long distance [4–6]. Based on the helical phase rotation Doppler effect [7], OAM beam was used for high-precision angular velocity measurement of rotating object [8,9]. Moreover, OAM beams was applied to enhance the sensing resolution of a fiber sensor through identifying the spiral interference pattern between OAM beam and spherical wave [10,11].

In these above studies on the OAM applications, the order of OAM modes is an important parameter. For example, the rotation speed of the trapped micro-particles in tweezer system is related to the order of OAM. The large-capacity optical communications directly multiplex OAM modes with different orders. Therefore, it is very important to generate different order OAM modes.

Currently, the OAM modes generators can be roughly divided into two categories. One is free-spatial generator system, such as mode converters [12], spatial light modulators [13], spiral phase plate [14], q-plates [15] and so on. These spatial generators have the advantages of mature technology and flexibility in practice, which provides a good support for the investigation of OAM beams. However, there are two common drawbacks for them, that is, high insertion loss

and large volume. Compared with free-spatial generators, the fiber-based ones [16–24] have the advantages of low insertion loss, small size, light weight, flexible use and complete compatibility with optical fiber communication system. Especially, the OAM mode generators based on fiber gratings have higher coupling efficiency and wavelength-selectivity, and thus, attract intensive attention. The OAM generators based on conventional long-period fiber gratings usually need other auxiliary equipments [18,25], such as pressure plate to realize the phase difference between modes participating in superposition, torsion device to change the light incident direction, or polarization controller to find the appropriate polarization state, which reduces the advantage in device size and stability. Meanwhile, the obtained OAM mode usually has a specific polarization state [26–28], which brings inconvenience to later use in practice. Recently, chiral long period fiber grating (CLPFG) [29,30], which can directly excite OAM mode without any assistant auxiliary, has been greatly developed. The typical fabrication method of CLPFG is to twist a section of hot melt fiber [31,32]. Using this method, 1<sup>st</sup>-order OAM mode generator with low insertion loss, high coupling efficiency, high purity and polarization independence is realized [33]. However, in this fabrication technology, the refractive index modulation of the obtained gratings is complex, and even unable to be adjusted. The improvement of grating coupling intensity can only be achieved by increasing the grating length. In symmetrical fiber, it needs strong grating modulation to realize higher-order ( $> 1$ ) OAM mode excitation [16,17]. Therefore, it is difficult to generate 2<sup>nd</sup>- and even higher-order OAM modes in CLPFG. Recently, Li et al. reported the excitation of 2<sup>nd</sup>- and 3<sup>rd</sup>-order OAM modes by using CLPFGs [34,35], which is a significant breakthrough in the study of OAM mode excited by CLPFGs. However, when the coupling efficiency of the obtained 2<sup>nd</sup>- and 3<sup>rd</sup>-order OAM modes are 95% and 98%, respectively, the grating length has been exceeded 4.75cm, and the insertion loss is up to 3dB. Thus, their grating quality needs to be further improved. At the same time, due to the difficulties in fabrication and the poor mode quality, the characteristics of higher-order OAM modes coupling are not further discussed.

In this paper, a class of ultra-short CLPFGs were realized by using CO<sub>2</sub> laser to write helical curves on the surface of a six-mode fiber. The fabrication technology avoids the operation of twisting the molten fiber and has better stability, and the CLPFG with only a few periods and ultra-short grating length can be realized by adjusting the laser power or exposure time. Experimentally, the higher-order OAM mode was flexibly designed and realized by adjusting the periodic parameters and the rotation direction of spiral curve. By optimizing the laser power, the CLPFG coupled the fundamental mode to  $\pm 2^{\text{nd}}$ - and  $\pm 3^{\text{rd}}$ -order OAM modes with a coupling efficiency over 99%, when it is only 0.5cm in length. Furthermore, the polarization characteristics of the coupled OAM modes were firstly theoretically analyzed by combining phase match condition of a fiber grating and conservation of angular momentum (AM), and then were confirmed in experiment.

## 2. Principle

Generally speaking, the excited higher-order OAM modes ( $l > 1$ ) can be expressed as a linear superposition of hybrid modes of  $\mathbf{HE}_{mn}^{\text{even/odd}} / \mathbf{EH}_{mn}^{\text{even/odd}}$  with a phase difference of  $\pi/2$ , respectively.  $\mathbf{HE}_{mn}^{\text{even,odd}}$  and  $\mathbf{EH}_{mn}^{\text{even,odd}}$  represent even or odd vector modes, respectively, which can be expressed by linearly polarized (LP) modes approximately in weakly guiding fibers. The subscripts  $m$  and  $n$  represent the angular and radial exponents of the vector modes, respectively. To better describe the higher-order OAM modes in CLPFGs, circular polarization (CP) mode is used as the basis [36,37], which is expressed as:

$$\mathbf{HE}_{mn}^{+} = (\mathbf{HE}_{mn}^{\text{even}} + i\mathbf{HE}_{mn}^{\text{odd}}) / \sqrt{2} \approx e^{i(m-1)\varphi} (\hat{x} + i\hat{y}) F_{m-1,n} / \sqrt{2}, \quad (1)$$

$$\mathbf{HE}_{mn}^{-} = (\mathbf{HE}_{mn}^{\text{even}} - i\mathbf{HE}_{mn}^{\text{odd}}) / \sqrt{2} \approx e^{-i(m-1)\varphi} (\hat{x} - i\hat{y}) F_{m-1,n} / \sqrt{2}, \quad (2)$$

$$\mathbf{EH}_{mn}^+ = (\mathbf{EH}_{mn}^{\text{even}} + i\mathbf{EH}_{mn}^{\text{odd}}) / \sqrt{2} \approx e^{i(m+1)\varphi} (\hat{x} - i\hat{y}) F_{m+1,n} / \sqrt{2}, \quad (3)$$

$$\mathbf{EH}_{mn}^- = (\mathbf{EH}_{mn}^{\text{even}} - i\mathbf{EH}_{mn}^{\text{odd}}) / \sqrt{2} \approx e^{-i(m+1)\varphi} (\hat{x} + i\hat{y}) F_{m+1,n} / \sqrt{2}, \quad (4)$$

where  $\mathbf{HE}_{mn}^\pm / \mathbf{EH}_{mn}^\pm$  is the OAM mode. The superscript of  $\mathbf{HE}_{mn}^\pm / \mathbf{EH}_{mn}^\pm$  represents the charge of spin angular momentum (SAM) denote by  $s = \pm 1$ .  $\hat{x} + i\hat{y}$  and  $\hat{x} - i\hat{y}$  represent left-handed circular polarization (LCP) and right-handed circular polarization (RCP), respectively, corresponding to  $s = +1$  and  $s = -1$ .  $F_{mn}$  symbolizes the radial wave functions of the  $\text{LP}_{mn}$  modes [38]. The total AM denoted by  $j$ , are the sums of OAM and SAM. The relationship among the SAM, OAM and total AM of the modes are summarized as shown in Table 1 when  $l = 0$ ,  $l = \pm 2$  and  $l = \pm 3$ . It is noted that, the relationship between the topological charge of OAM modes and the angular components  $m$  of vector modes meets  $l = m - 1$  for  $\mathbf{HE}_{mn}^\pm$  and  $l = m + 1$  for  $\mathbf{EH}_{mn}^\pm$ . As a results, there are two degenerate modes for each orbital angular momentum mode  $l = 0, -2, +2, -3, +3$ . Because the total AM denoted by  $j$ , is the sum of OAM and SAM, the total AM distribution of each degenerate mode can be intuitively expressed in the Table 1 below.

**Table 1. Charges of the SAM, OAM and total AM in CLPFG when  $l=0, l=\pm 2, l=\pm 3$**

Modes	$\mathbf{HE}_{11}^+$	$\mathbf{HE}_{11}^-$	$\mathbf{HE}_{31}^+$	$\mathbf{HE}_{31}^-$	$\mathbf{EH}_{11}^+$	$\mathbf{EH}_{11}^-$	$\mathbf{HE}_{41}^+$	$\mathbf{HE}_{41}^-$	$\mathbf{EH}_{21}^+$	$\mathbf{EH}_{21}^-$
$s$	+1	-1	+1	-1	-1	+1	+1	-1	-1	+1
$l$	0	0	+2	-2	+2	-2	+3	-3	+3	-3
$j$	+1	-1	+3	-3	+1	-1	+4	-4	+2	-2

In CLPFG, the mode coupling between the fundamental mode ( $l=0$ ) and higher-order OAM modes needs to follow phase matching condition of a grating and conservation of AM [39]. At the same time, the fabrication of CLPFG is imperfect, which results the inhomogeneous of azimuthal modulation. Thus, the azimuthal distribution of refractive index modulation includes not only low-order harmonic terms, but also the higher-order harmonic terms [34]. Therefore, the phase matching condition and conservation of AM can be modified as:

$$n_f - n_h = q \cdot (\lambda / \Lambda), \quad (5)$$

$$j_f - j_h + q \cdot C = 0, \quad (6)$$

where  $n_f$ ,  $n_h$  and  $j_f$ ,  $j_h$  represents the effective refractive index and total AM of the fundamental mode and higher-order mode, respectively.  $q$  represents the order of harmonic term, and the value of  $q$  determines the topological charge number of excited OAM mode in CLPFGs.  $\Lambda$  is the pitch of CLPFG.  $C$  represents the rotational symmetry of the grating modulation cross section which meet  $C = \pm 1$  in this work, because the optical fiber used is axisymmetric.  $C = +1$  and  $C = -1$  represent the left-handed CLPFG (L-CLPFG) and right-handed CLPFG (R-CLPFG), respectively.

To satisfy the mode coupling conditions from  $l = 0$  to  $l = \pm 2$  and  $l = 0$  to  $l = \pm 3$ , the  $q$  is taken as 2 and 3. The corresponding mode matching is shown in Table 2.

**Table 2. Mode coupling matching from fundamental mode to the 2<sup>nd</sup>- and 3<sup>rd</sup>-order OAM mode in CLPFGs involving OAM and SAM**

Fundamental Mode	OAM Mode ( $l = \pm 2, q = 2$ )		OAM Mode ( $l = \pm 3, q = 3$ )	
	L-CLPFG	R-CLPFG	L-CLPFG	R-CLPFG
$\mathbf{HE}_{11}^+$	$\mathbf{HE}_{31}^+$	$\mathbf{EH}_{11}^-$	$\mathbf{HE}_{41}^+$	$\mathbf{EH}_{21}^-$
$\mathbf{HE}_{11}^-$	$\mathbf{EH}_{11}^+$	$\mathbf{HE}_{31}^-$	$\mathbf{EH}_{21}^+$	$\mathbf{HE}_{41}^-$

When  $q = 2$ , the fundamental mode can be coupled to  $\pm 2^{\text{nd}}$ -order OAM mode by using CLPFGs. In L-CLPFG, the  $\mathbf{HE}_{11}^+$  mode ( $l = 0, s = +1$ ) is coupled to the  $\mathbf{HE}_{31}^+$  mode ( $l = +2, s = +1$ ) and

the  $\mathbf{HE}_{11}^-$  mode ( $l=0, s=-1$ ) is coupled to  $\mathbf{EH}_{11}^+$  mode ( $l=+2, s=-1$ ). In R-CLPFG, mode ( $l=0, s=+1$ ) is coupled to the  $\mathbf{EH}_{11}^-$  mode ( $l=-2, s=+1$ ) and the  $\mathbf{HE}_{11}^-$  mode ( $l=0, s=-1$ ) is coupled to  $\mathbf{HE}_{31}^-$  mode ( $l=-2, s=-1$ ). Similarly, when  $q=3$ , the fundamental mode can be coupled to  $\pm 3^{\text{rd}}$ -order OAM mode in CLPFGs. In L-CLPFG, the  $\mathbf{HE}_{11}^+$  mode ( $l=0, s=+1$ ) is coupled to the  $\mathbf{HE}_{41}^+$  mode ( $l=+3, s=+1$ ) and the  $\mathbf{HE}_{11}^-$  mode ( $l=0, s=-1$ ) is coupled to  $\mathbf{EH}_{21}^+$  mode ( $l=+3, s=-1$ ). In R-CLPFG,  $\mathbf{HE}_{11}^+$  mode ( $l=0, s=+1$ ) is coupled to the  $\mathbf{EH}_{21}^-$  mode ( $l=-3, s=+1$ ) and the  $\mathbf{HE}_{11}^-$  mode ( $l=0, s=-1$ ) is coupled to  $\mathbf{HE}_{41}^-$  mode ( $l=-3, s=-1$ ). As shown in Table 2, the fundamental mode with  $s=+1$  is always coupled to the higher-order OAM mode with  $s=+1$  while with  $s=-1$  always coupled to the higher-order OAM with  $s=-1$ . The “ $\pm$ ” of  $l$  depends on the helicity of CLPFGs. Therefore, the charge of AM and OAM change correspondingly with the mode coupling in CLPFG while the charge of SAM keep unchanged. The polarization selection characteristic is involved here. The linear polarization (LP) state light can be regarded as the superposition of LCP and RCP light with the same amplitude. When the fundamental mode with LP state, LCP state and RCP state are input into CLPFGs, respectively, the higher-order OAM modes with the same polarization state are excited.

Therefore, in CLPFGs, the polarization selectivity comes from phase matching condition and conservation of AM, and the excited OAM modes are polarization independent.

### 3. Experimental results and discussion

The optical fiber used in this work is six-mode fiber with a step-index profile. The fiber end face was observed by optical microscope and recorded in Fig. 1(a). The two dimensional refractive index profile of this fiber was measured by an optical fiber refractive index analyzer at the wavelength of 1550nm, as was shown in Fig. 1(b) and (c). There are four-layer structure distributed on the crossing section of the optical fiber, containing fiber core, inner cladding, restrain layer and outer cladding. The radius of the fiber core, inner and outer of the suppression layer, and the cladding are 8.0 $\mu\text{m}$ , 13.5 $\mu\text{m}$ , 17.5 $\mu\text{m}$  and 62.5 $\mu\text{m}$ . And the corresponding refractive index of the four layers from inside to outside are 1.45601, 1.46693, 1.45018 and 1.46693, respectively. The effective refractive index of the vector modes supported by six-mode fiber are calculated by using these parameters above and finite element algorithm in the wavelength range from 1250 nm to 1700 nm. Substituting the calculated results into Eq. (5), the dispersion curve of resonant wavelength with respect to grating pitch was calculated for the mode coupling from  $\mathbf{HE}_{11}^+$  to  $\mathbf{HE}_{31}^+/\mathbf{HE}_{41}^+$  and from  $\mathbf{HE}_{11}^-$  to  $\mathbf{EH}_{11}^+/\mathbf{EH}_{21}^+$  as is depicted in Fig. 1(d).

The CLPFG was fabricated by curving spiral lines along the fiber axis, which was achieved by simultaneously rotating and translating the fiber while the light from the CO<sub>2</sub> laser is focused on the fiber cladding. The grating modulation mainly resulting from residual stress release around the spiral curves area can be designed by adjusting the laser power, and the grating pitch can be adjusted by changing the speed of fiber rotation and translation. The detailed description about the fabrication technology can be referred to Ref. [40]. The sketch of the fabricated CLPFG is shown in Fig. 2(a). Figure 2(b) and (c) show the photographs of the obtained L-CLPFG and R-CLPFG. The etching traces on L-CLPFG and R-CLPFG were clearly observed, and the etching depth was about 4.8 $\mu\text{m}$ . With the increase of CO<sub>2</sub> laser energy, the modulation intensity of the grating increases, the grating length becomes shorter, but the insertion loss increases and the etching depth deepens. Thus, it is necessary to select the appropriate energy to fabricate CLPFGs in the experiment.

According to Fig. 1(d), the grating pitch of 600 $\mu\text{m}$  and 660 $\mu\text{m}$  were selected to excite 3<sup>rd</sup>- and 2<sup>nd</sup>-order OAM modes, respectively. The transmission spectra of the CLPFGs were recorded by an optical spectrum analyzer, combined with an amplified spontaneous emission broadband light source. Under the laser power of 250mW, the CLPFG1 with a pitch of 600 $\mu\text{m}$  was achieved at a length of only 0.5cm, and the coupling efficiency was up to 99% as shown in Fig. 2(d). The resonant wavelength and dip loss were 1540.6 nm and 20.97 dB for L-CLPFG1, and were 1541.2

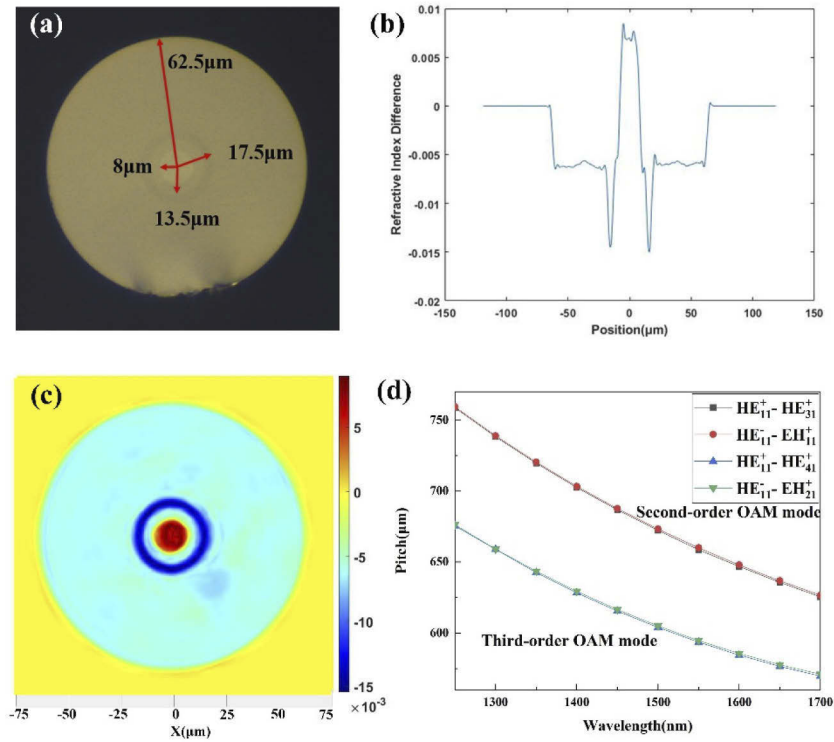


**Fig. 1.** (a) The fiber end face observed by optical microscope; (b) the transverse refractive index profile of the six-mode index-step fiber; (c) refractive index distribution of fiber cross section (d) dispersion curve of resonant wavelength with respect to grating pitch for coupling the fundamental mode  $HE_{11}^{\pm}$  to  $\pm 2^{nd}$ - and  $\pm 3^{rd}$ -order OAM modes.

nm and 22.20dB for R-CLPFG1, respectively. The 3dB bandwidth of L-CLPFG was 154.2nm and R-CLPFG was 159.9nm. The slight differences in resonant wavelength, dip loss and 3dB bandwidth may come from the error of the optical fiber rotators and the translation stages in the process of synchronous matching. Figure 2(e) depicts the transmission spectra of CLPFG2 with a pitch of 660μm. The resonant wavelength and dip loss were 1582.5nm and 21.85 dB for L-CLPFG2, and were 1582.4 nm and 22.80dB for R-CLPFG2, respectively. The 3dB bandwidth of L-CLPFG was 182.7nm and R-CLPFG was 167.5nm. The used laser power was 233mW, and the obtained grating length was only 0.7cm. The PDL of the prepared CLPFGs were lower than 5.5dB, which had no effect on the excitation of helical phase and caused the fluctuation of mode purity under different polarization states. Compared with the fabrication technology based on twisting fused fiber, this processing technology of CLPFG requires lower laser power, and possesses better stability, repeatability and flexibility.

The excitation of helical phase in CLPFG was firstly investigated. To confirmed the helical phase excited by CLPFG, the co-axis interference method was used. The schematic diagram of the experimental setup is shown in Fig. 3(a). The light from a tunable laser with a wavelength range of 1450nm-1650nm was split into two beams by a 3dB coupler. One beam was collimated by a 20× objective lens, coupled into the CLPFG, and meet and interfered with the other path of light at a beam combiner. The interference pattern was observed and recorded by a CCD. When the path of light without CLPFG was blocked, the intensity distribution of coupled mode can be obtained.



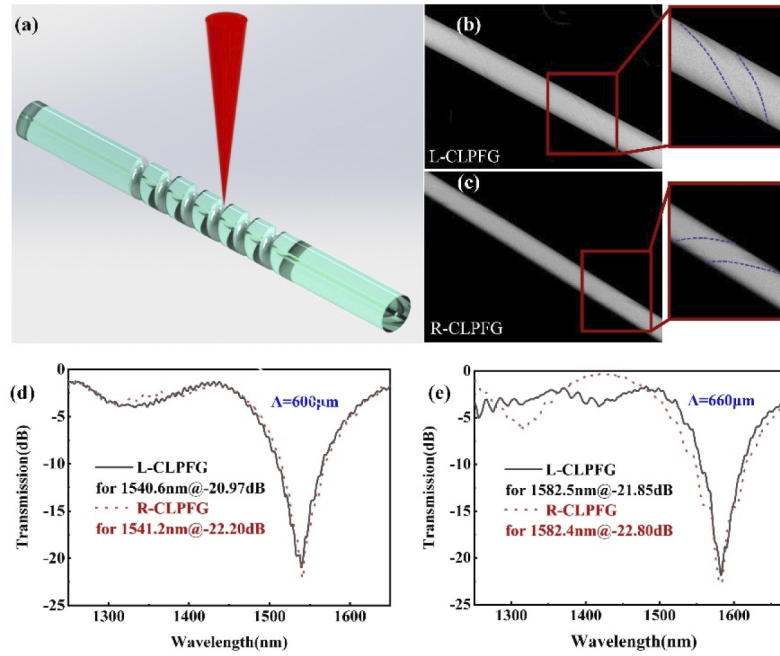


**Fig. 2.** (a) The fabrication setup diagrammatic sketch of CLPFG; the structure of (b) L-CLPFG and (c) R-CLPFG observed by SEM; (d) the measured transmission of CLPFG1 with  $\Lambda=600\mu\text{m}$ ; (e) the measured transmission of CLPFG2 with  $\Lambda=660\mu\text{m}$ ; solid lines: L-CLPFG; dotted line: R-CLPFG.

Figure 3(b) and (c) shows the intensity distributions of modes excited by L-CLPFG1 and R-CLPFG1 at the resonant wavelength, respectively. The typical donut-shaped intensity profiles are confirmed. The spiral interference patterns shown in Fig. 3(f) and (g) corresponding to the Fig. 3(b) and (c), verified the generation of  $+3^{\text{rd}}$ - and  $-3^{\text{rd}}$ -order OAM modes. The experiment results agree well with the theoretical analysis in Table 2 and simulation result in the Fig. 1(d).

Similarly, we investigate the L-CLPFG2 and R-CLPFG2 using the same setup. Figure 3(d), (e), (h) and (i) show the intensity distribution of the coupled modes and the corresponding interference patterns at the resonance wavelength respectively. Results confirmed the excitation of  $\pm 2^{\text{nd}}$ -order OAM modes.

Furthermore, the  $+l$  order OAM modes were excited in L-CLPFG and the  $-l$  order OAM modes were excited in R-CLPFG, which was conformed to the theoretical analysis in Table 2.

The polarization characteristics were investigated as well. Some polarization elements were inserted into the experiment setup in Fig. 3(a). Polarizer 1(P1) and quarter-wave plate 1(QWP1) were used to generate arbitrary polarization states of the incident light by adjusting the angle between them. Polarizer 2(P2) was used to analyze the polarization state of the OAM beam excited by CLPFG. Quarter-wave plate 2(QWP2) was used to convert circularly polarized light into LP light. Meanwhile, the CP state and its rotation direction were analyzed through the combination of P2 and QWP2. Polarizer 3(P3) was used to purify the reference light. Half wave plate 1(HWP1) and half wave plate 2(HWP2) were used to rotate the linear polarization direction. The intensity of the reference light could be changed by neutral density filters (NDF).

The changes of intensity distribution and interference patterns of  $\pm 3^{\text{rd}}$ -order OAM modes were studied and recorded in Fig. 4(a) and (b) under different polarization states of input light.  $\text{LP}^{\parallel}$  and  $\text{LP}^{\perp}$  represented LP state of input light whose vibration direction was parallel and perpendicular to the transparent axis of P1, respectively, and they were generated by P1 and the

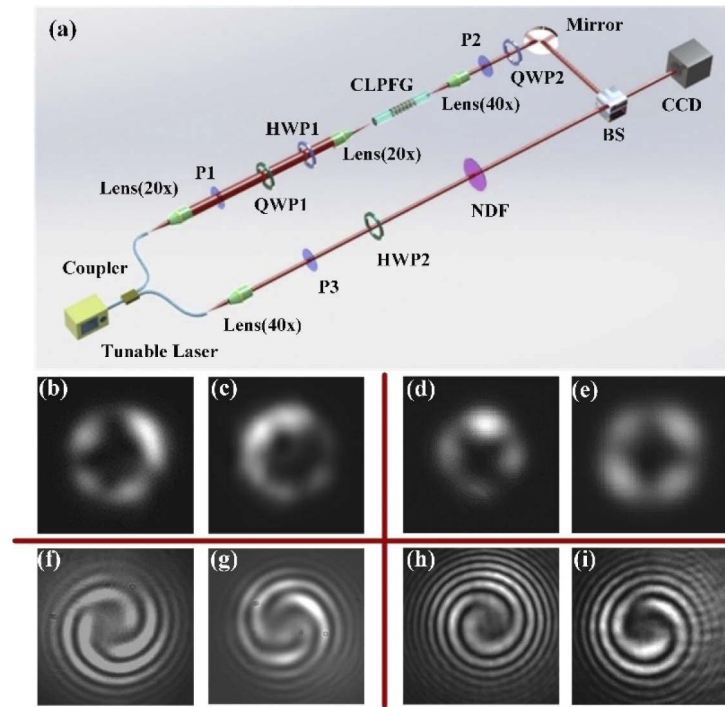


**Fig. 3.** (a) Schematic diagram of experimental setup for measuring the intensity and phase of the OAM modes excited in CLPFGs; (b)–(e) and (f)–(i) are the intensity distributions and interference patterns of the OAM modes with  $l = +3, -3, +2$ , and  $-2$ , respectively; P1 and P2, polarizer; QWP1 and QWP2, quarter-wave plate; HWP1 and HWP2, half-wave plate; NDF, neutral density filters; BS, beam splitter.

followed HWP1. The LCP state and RCP state of input light were generated by adjusting the angle to be  $\pm 45^\circ$  between the transparent axis of P1 and the optical axis of QWP1. By rotating P2 at a  $90^\circ$  intervals, we study the intensity distribution and interference pattern changes of OAM mode under different polarization input light. It is note that, the starting position  $0^\circ$  for testing was the angle of the P2 with the highest light transmittance when  $LP^\parallel$  was applied in experiment.

When the input light is applied with  $LP^\parallel$  and  $LP^\perp$ , intensity distributions change of excited  $\pm 3^{\text{rd}}$ -order OAM modes were shown in Fig. 4(a<sub>11</sub>), (a<sub>21</sub>) for L-CLPFG1 and in Fig. 4(b<sub>11</sub>) and (b<sub>21</sub>) for R-CLPFG1, respectively. The intensity of light periodically changed with an obvious extinction phenomenon in the rotating process of P2. The corresponding interference patterns were plotted in Fig. 4(a<sub>12</sub>), (a<sub>22</sub>), (b<sub>12</sub>) and (b<sub>22</sub>). Only the reference light was captured when the OAM beams to be measured were in extinction state. The test resulted showed that the helical phase was excited under different LP states of input light, and the OAM mode was still LP state.

When the input light with LCP and RCP states were applied, respectively, the intensity distributions and the corresponding interference patterns were plotted in Fig. 4(a<sub>31</sub>)–(a<sub>42</sub>) for L-CLPFG1 and (b<sub>31</sub>)–(b<sub>42</sub>) for R-CLPFG1. Both of them kept constant in the rotating process of P2, which indicated that the obtained OAM beams were CP state as well.

The CP state and its rotation direction of the output light were verified by adjusting angle between QWP2 and P2. The measured results in Fig. 5 showed that the CP state of  $\pm 3^{\text{rd}}$ -order OAM modes were converted into LP state by QWP2. When LCP light was injected into CLPFGs, the output light was converted into LP state through QWP2. As is shown in Fig. 5(a<sub>11</sub>), (a<sub>12</sub>), (b<sub>11</sub>) and (b<sub>12</sub>), the intensity of LP light changed periodically from bright to dark and the interference

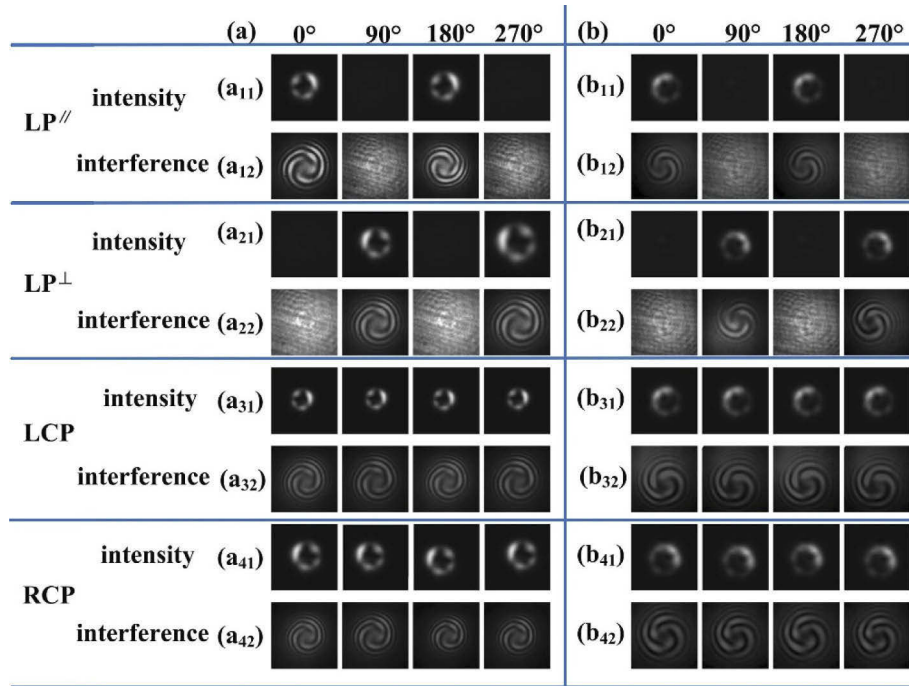


**Fig. 4.** Polarization characteristic analysis of (a) the +3<sup>rd</sup>-order OAM mode excited by the L-CLPFG1 and (b) the -3<sup>rd</sup>-order OAM mode excited by the R-CLPFG1 at the resonant wavelength. The leftmost column shows the input light with different polarization states.

pattern changed together with intensity as P2 rotated clockwise, which means that the output light from CLPFGs still kept LCP state. For RCP input light shown in Fig. 5(a<sub>21</sub>), (a<sub>22</sub>), (b<sub>21</sub>) and (b<sub>22</sub>), the intensity of LP light changed periodically from dark to bright and the interference pattern changed together with intensity as P2 rotates clockwise, which mean the output light from CLPFGs still kept RCP state. The above results showed that the CP state and its rotation direction of the excited  $\pm 3^{\text{rd}}$ -order OAM modes in CLPFGs was consistent with that of input light, which was consistent with Table 2.

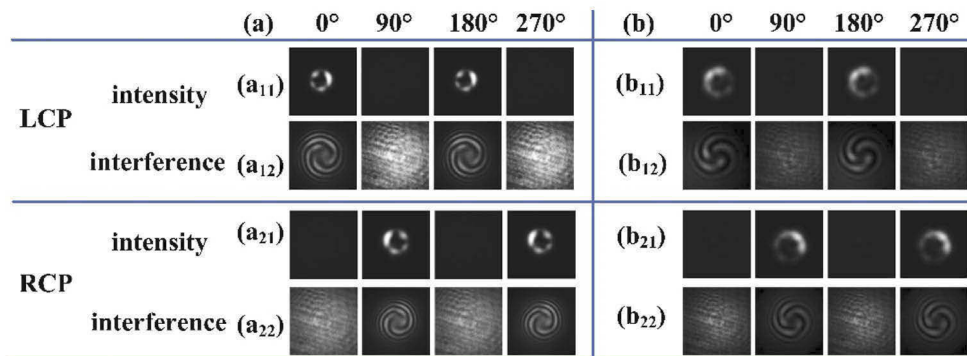


**Fig. 5.** Analysis about the CP state and its rotation direction of  $\pm 3^{\text{rd}}$ -order OAM modes excited in (a) L-CLPFG1 and (b) R-CLPFG1.



Similarly, the polarization characteristics of 2<sup>nd</sup>-order OAM modes were measured as well. As shown in Fig. 6 and Fig. 7, the results were consistent with that of  $\pm 3^{\text{rd}}$ -order OAM modes in Fig. 4 and Fig. 5. The CP state and its rotation direction of  $\pm 2^{\text{nd}}$ -order OAM modes kept unchanged. The polarization characteristics of  $\pm 2^{\text{nd}}$ -order OAM modes excited in CLPFGs were consistent with  $\pm 3^{\text{rd}}$ -order OAM modes, which confirmed that the phase matching condition of Eq. (5) and conservation of AM of Eq. (6) suitable for the coupling of OAM modes in Table 2.

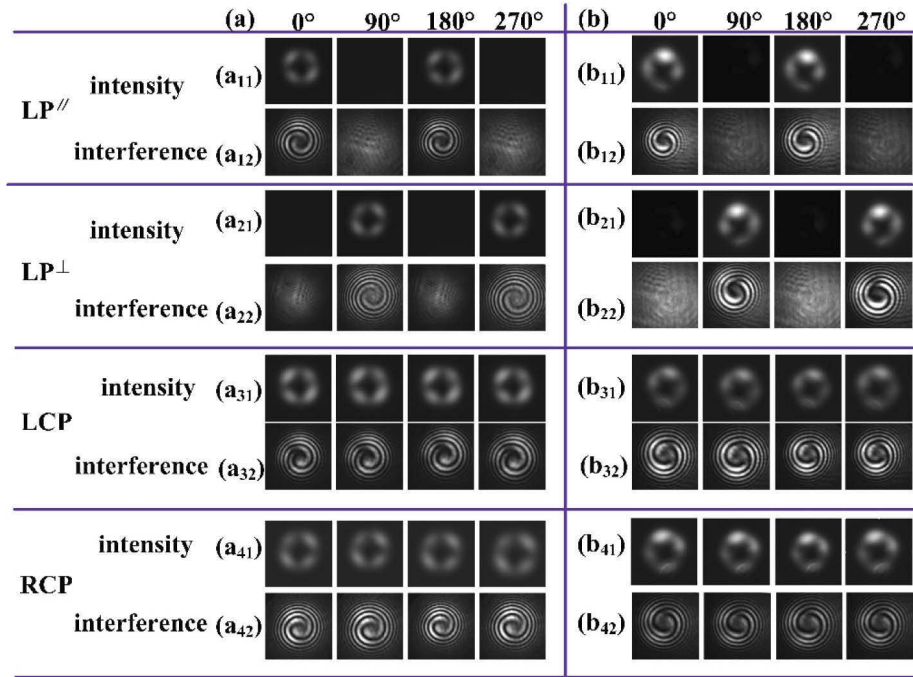


**Fig. 6.** For LP<sup>||</sup>, LP<sup>⊥</sup>, LCP and RCP input light, the intensity and interference patterns of the  $\pm 2^{\text{nd}}$ -order OAM mode excited by (a) the L-CLPFG2 and (b) R-CLPFG2 with pitch of 660 $\mu\text{m}$ , respectively.

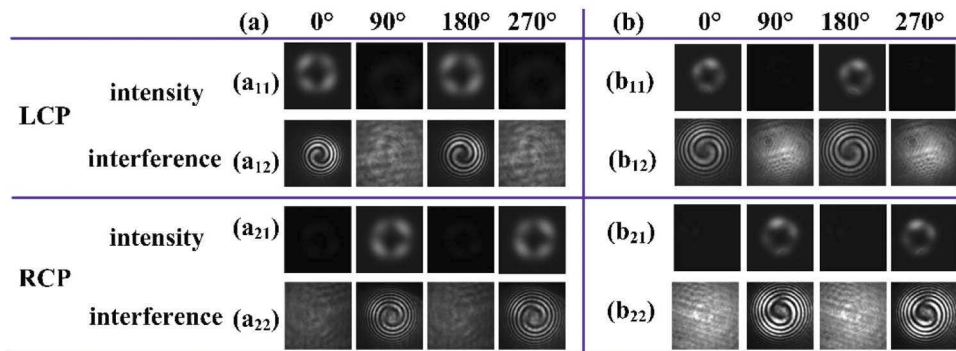


**Fig. 7.** Analysis about circular polarization state and its rotation direction of  $\pm 2^{\text{nd}}$ -order OAM modes excited in (a) L-CLPFG2 and (b) R-CLPFG2, respectively.

#### 4. Conclusion

The ultra-short CLPFGs with a length less than 1cm have been realized by using CO<sub>2</sub> laser to write spiral curve on the surface of a fiber. The small-size of the obtained CLPFGs are more conducive to integrated application. The  $\pm 2^{\text{nd}}$ - and  $\pm 3^{\text{rd}}$ -order OAM modes have been excited in the CLPFGs with a coupling efficiency of more than 99%, which is a much better results compared with the previous works. Through the theoretical analysis and experimental verification, the polarization characteristics of the  $\pm 2^{\text{nd}}$ - and  $\pm 3^{\text{rd}}$ -order OAM modes are independent from the helicity of the CLPFGs and only related to the polarization state of the incident light. And thus, the independent modulation of OAM and polarization of a light beam is realized, which brings great convenience to the application of OAM beams.

**Funding.** National Natural Science Foundation of China (61875134, 61905155, 62005169); Shenzhen Science and Technology Innovation Program (JCYJ20180507182058432); Shenzhen University (grant no. 2019097).

**Disclosures.** The authors declare no conflicts of interest.

**Data availability.** Data underlying the results presented in this paper are not publicly available at this time but may be obtained from the authors upon reasonable request.

#### References

1. Z. Shen, Z. Xiang, Z. Wang, Y. Shen, and B. Zhang, "Optical spanner for nanoparticle rotation with focused optical vortex generated through a Pancharatnam–Berry phase metalens," *Appl. Opt.* **60**(16), 4820–4826 (2021).
2. R. S. Aspden, P. A. Morris, R. He, Q. Chen, and M. J. Padgett, "Heralded phase-contrast imaging using an orbital angular momentum phase-filter," *J. Opt.* **18**(5), 055204 (2016).
3. S. R. Ghaleh, S. A. Kandjani, R. Kherradmand, and B. Olyaeefar, "Improved edge detection in computational ghost imaging by introducing orbital angular momentum," *Appl. Opt.* **57**(32), 9609–9614 (2018).
4. R. G. Zhu, Z. Hu, X. Wu, C. Du, W. Luo, Y. Chen, X. Cai, J. Liu, J. Zhu, and S. Yu, "Scalable mode division multiplexed transmission over a 10-km ring-core fiber using higher-order orbital angular momentum modes," *Opt. Express* **26**(2), 594–604 (2018).
5. C. Brunet, P. Vaity, Y. Messaddeq, S. Larochelle, and L. A. Rusch, "Design, fabrication and validation of an OAM fiber supporting 36 states," *Opt. Express* **22**(21), 26117–26127 (2014).
6. G. Zhu, Y. Chen, X. Cai, J. Liu, Y. Zhang, and S. Yu, "Characterizing a  $14 \times 14$  OAM mode transfer matrix of a ring-core fiber based on quadrature phase-shift interference," *Opt. Lett.* **42**(7), 1257–1261 (2017).
7. L. Allen, M. Babiker, and W. L. Power, "Azimuthal Doppler shift in light beams with orbital angular momentum," *Opt. Commun.* **112**(3-4), 141–144 (1994).
8. M. P. J. Lavery, F. C. Speirits, S. M. Barnett, and M. J. Padgett, "Detection of a spinning object using light's orbital angular momentum," *Science* **341**(6145), 537–540 (2013).
9. J. Courtial, K. Dholakia, D. A. Robertson, L. Allen, and M. J. Padgett, "Measurement of the Rotational Frequency Shift Imparted to a Rotating Light Beam Possessing Orbital Angular Momentum," *Phys. Rev. Lett.* **80**(15), 3217–3219 (1998).
10. L. Qiu, H. Hu, Y. Zhao, J. Li, and Q. Wang, "Fiber optic temperature sensor using the orbital angular momentum and gaussian beams," *Instrum. Sci. Technol.* **45**(2), 123–136 (2017).
11. F. Pang, H. Zheng, H. Liu, J. Yang, N. Chen, Y. Shang, S. Ramachandran, and T. Wang, "The Orbital Angular Momentum Fiber Modes for Magnetic Field Sensing," *IEEE Photonics Technol. Lett.* **31**(11), 893–896 (2019).
12. J. Arlt and K. Dholakia, "Generation of higher-order Bessel beams by use of an axicon," *Opt. Commun.* **177**(1-6), 297–301 (2000).
13. N. R. Heckenberg, R. McDuff, C. P. Smith, and A. G. White, "Generation of optical phase singularities by computer-generated holograms," *Opt. Lett.* **17**(3), 221–223 (1992).
14. J. M. Otón, E. Otón, X. Quintana, and M. A. Geday, "Liquid-crystal phase-only devices," *J. Mol. Liq.* **267**, 469–483 (2018).
15. L. Marrucci, C. Manzo, and D. Paparo, "Optical spin-to-orbital angular momentum conversion in inhomogeneous anisotropic media," *Phys. Rev. Lett.* **96**(16), 163905 (2006).
16. H. Wu, S. Gao, B. Huang, Y. Feng, X. Huang, W. Liu, and Z. Li, "All-fiber second-order optical vortex generation based on strong modulated long-period grating in a four-mode fiber," *Opt. Lett.* **42**(24), 5210–5213 (2017).
17. X. He, J. Tu, X. Wu, S. Gao, L. Shen, C. Hao, Y. Feng, W. Liu, and Z. Li, "All-fiber third-order orbital angular momentum mode generation employing an asymmetric long-period fiber grating," *Opt. Lett.* **45**(13), 3621–3624 (2020).
18. R. D. Niederritter, M. E. Siemens, and J. T. Gopinath, "Continuously tunable orbital angular momentum generation using a polarization-maintaining fiber," *Opt. Lett.* **41**(14), 3213–3216 (2016).
19. P. S. Russell, R. Beravat, and G. K. Wong, "Helically twisted photonic crystal fibres," *Philos. Trans. R. Soc. A.* **375**(2087), 20150440 (2017).

20. Y. Li, Z. Bai, Z. Liu, G. Zhu, K. Yang, J. Yu, J. Chen, C. Fu, C. Liao, and Y. Wang, "High purity optical vortex generation in a fiber Bragg grating inscribed by a femtosecond laser," *Opt. Lett.* **45**(24), 6679–6682 (2020).
21. Y. Zhao, Y. Liu, J. Wen, and T. Wang, "Mode converter based on the long-period fiber gratings written in the two-mode fiber," *Opt. Express* **24**(6), 6186–6195 (2016).
22. S. Pidishety, S. Pachava, P. Gregg, S. Ramachandran, G. Brambilla, and B. Srinivasan, "Orbital angular momentum beam excitation using an all-fiber weakly fused mode selective coupler," *Opt. Lett.* **42**(21), 4347–4350 (2017).
23. Z. Liu, G. Zhu, Y. Li, J. Yu, Z. Bai, S. Liu, J. He, and Y. Wang, "Orthogonal long-period fiber grating for directly exciting the orbital angular momentum," *Opt. Express* **28**(18), 27044–27051 (2020).
24. J. Yu, C. Fu, Z. Bai, and Y. Wang, "Super-Variable Focusing Vortex Beam Generators Based on Spiral Zone Plate Etched on Optical Fiber Facet," *J. Lightwave Technol.* **39**(5), 1416–1422 (2021).
25. S. Li, Q. Mo, X. Hu, C. Du, and J. Wang, "Controllable all-fiber orbital angular momentum mode converter," *Opt. Lett.* **40**(18), 4376–4379 (2015).
26. Y. Han, Y. Liu, Z. Wang, W. Huang, L. Chen, H. Zhang, and K. Yang, "Controllable all-fiber generation/con-version of circularly polarized orbital angular momentum beams using long period fiber gratings," *Nanophotonics* **7**(1), 287–293 (2018).
27. Y. Jiang, G. Ren, W. Jin, Y. Xu, W. Jian, and S. Jian, "Polarization properties of fiber-based orbital angular momentum modes," *Opt. Fiber. Technol.* **38**, 113–118 (2017).
28. Y. Jiang, G. Ren, Y. Shen, Y. Xu, W. Jin, Y. Wu, W. Jian, and S. Jian, "Two-dimensional tunable orbital angular momentum generation using a vortex fiber," *Opt. Lett.* **42**(23), 5014–5017 (2017).
29. G. K. L. Wong, M. S. Kang, H. W. Lee, F. Biancalana, C. Conti, T. Weiss, and P. S. J. Russell, "Excitation of Orbital Angular Momentum Resonances in Helically Twisted Photonic Crystal Fiber," *Science* **337**(6093), 446–449 (2012).
30. C. Fu, B. Yu, Y. Wang, S. Liu, Z. Bai, J. He, C. Liao, Y. Wang, Z. Li, Y. Zhang, and K. Yang, "Orbital Angular Momentum Mode Converter Based on Helical Long Period Fiber Grating Inscribed by Hydrogen–Oxygen Flame," *J. Lightwave Technol.* **36**(9), 1683–1688 (2018).
31. C. Fu, S. Liu, Y. Wang, Z. Bai, J. He, C. Liao, Y. Zhang, F. Zhang, B. Yu, S. Gao, Z. Li, and Y. Wang, "Higher-order orbital angular momentum mode generator based on twisted photonic crystal fiber," *Opt. Lett.* **43**(8), 1786–1789 (2018).
32. L. Xian, P. Wang, and H. Li, "Power-interrogated and simultaneous measurement of temperature and torsion using paired helical long-period fiber gratings with opposite helicities," *Opt. Express* **28**(8), 11990–12000 (2020).
33. Y. Zhang, Z. Bai, C. Fu, S. Liu, J. Tang, J. Yu, C. Liao, Y. Wang, J. He, and Y. Wang, "Polarization-independent orbital angular momentum generator based on a chiral fiber grating," *Opt. Lett.* **44**(1), 61–64 (2019).
34. H. Zhao, P. Wang, T. Yamakawa, and H. Li, "All-fiber second-order orbital angular momentum generator based on a single-helix helical fiber grating," *Opt. Lett.* **44**(21), 5370–5373 (2019).
35. T. Detani, H. Zhao, P. Wang, T. Suzuki, and H. Li, "Simultaneous generation of the second- and third-order OAM modes by using a higher-order helical long-period fiber grating," *Opt. Lett.* **46**(5), 949–952 (2021).
36. K. Ren, L. Ren, J. Liang, L. Yang, J. Xu, D. Han, Y. Wang, J. Liu, J. Dong, H. He, and W. Zhang, "Excitation of high-quality orbital angular momentum vortex beams in an adiabatically helical-twisted single-mode fiber," *Opt. Express* **29**(6), 8441–8450 (2021).
37. H. Xu and L. Yang, "Conversion of orbital angular momentum of light in chiral fiber gratings," *Opt. Lett.* **38**(11), 1978–1980 (2013).
38. N. Bozinovic, S. Golowich, P. Kristensen, and S. Ramachandran, "Control of orbital angular momentum of light with optical fibers," *Opt. Lett.* **37**(13), 2451–2453 (2012).
39. M. Napiorkowski and W. Urbanczyk, "Role of symmetry in mode coupling in twisted microstructured optical fibers," *Opt. Lett.* **43**(3), 395–398 (2018).
40. Z. Bai, Y. Wang, Y. Zhang, C. Fu, S. Liu, M. Li, C. Liao, Y. Wang, and J. He, "Helical Long-Period Fiber Gratings as Wavelength-Tunable Orbital Angular Momentum Mode Generators," *IEEE Photonics Technol. Lett.* **32**(7), 418–421 (2020).